Visualization of acceleration in multiphase fluid interactions

Visualization of acceleration in multiphase fluid interactions

DAVID SEDARSKY[1,*], MATTIAS RAHM[1], AND MARK LINNE[2]

[1] Applied Mechanics, Chalmers University of Technology, SE-41296, Gothenburg, Sweden
[2] School of Engineering, University of Edinburgh, Mayfield Road, Edinburgh, EH9 3DW, UK
[*] Corresponding author: sedarsky@chalmers.se

Compiled February 22, 2016

Probing the dynamics of structures in turbid media is important for understanding the internal forces which drive the time-evolution of many fluid systems; the breakup of fuel injection sprays is a prime example. We demonstrate a three-pulse configuration for time-gated ballistic imaging, applied to a turbulent, steady spray allowing the acquisition of time-correlated image data. Coupled with targeted region-matching analysis, the detected image-triplets are used to generate time-resolved velocity and acceleration vectors representing motion and forces involved in spray development.

OCIS codes: *(120.7250) Velocimetry; (110.0113) Imaging through turbid media; (190.3270) Kerr effect.*

http://dx.doi.org/10.1364/ao.XX.XXXXXX

Turbid environments present challenges to optical diagnostics, limiting the available signal and contributing scattered-light noise that must be mitigated to provide the contrast necessary to resolve hidden internal structures. In high turbidity measurement volumes, like those important for in-vivo biological processes or multiphase fluid mixing, multiply-scattered photons dominate the collected light. The turbid volume significantly changes the character of the optical signal, altering the scattered intensities and apparent interaction cross-section, as well as correlations of the collected light [1]. This complicates analysis in measurements which use the scattered-light signal, as trends and relations developed from the highly transmissive case (e.g. Beer's law) cannot be strictly applied [2, 3]. While standard visible light imaging methods are severely degraded in the presence of strong scattering, a variety of filtering approaches (often termed "ballistic imaging" methods) have been applied with success to image structure within optically dense measurement regions. Some notable examples include optical mammography [4], investigation of lipid interfaces by two-photon fluorescence [5], holography for resolving microfluidic mixing layers [6], and optical Kerr effect time-gating to reveal fuel spray breakup behavior [7].

While much of the early work in ballistic imaging (BI) was focused on medical diagnostics, there is currently a renewed interest in exploiting time-gating BI variants in light of their suitability for probing fuel injection and similar multiphase fluid interactions. Despite the widespread industrial use of sprays (e.g., material deposition, cutting, and mixing), the design and testing of most spray devices remains largely phenomenological, due in part to limitations in computing power, but also to gaps in the fundamental understanding of multiphase fluid phenomena which drive spray breakup and morphology [8].

A prime objective for developing a first-principles understanding of sprays is enabling measurements in turbid spray regions, especially those which can lend insight into fluid motion and the forces active in spray mixing. This work presents such an approach, imaging the liquid-gas interface of a spray where shear forces and turbulence instabilities act to break the liquid apart. Subsequent region matching analysis is applied to this time-correlated image data in order to compute the velocity and acceleration of resolved fluid structures.

The three-pulse time-gated ballistic imaging measurement relies on intense ultrafast light pulses and specialized detection to separate high-quality imaging light from the diffusely scattered background light. Measurement data are obtained by illuminating the region of interest with a series of coherent ultrafast pulses generated from a single Ti:Sapphire oscillator (Spectra Physics, Mai Tai) which seeds three matched regenerative amplifiers (Spectra Physics, Spitfire Pro). This arrangement yields $\sim$3 mJ pulses with widths of $\sim$100 fs, centered on 800 nm with a $1/e^2$ beam diameter of $\sim$8 mm (see fig. 1). Here, the intra-pulse spacing of the pulse train is determined by the control timing of the Nd:YLF pump lasers (Spectra Physics, Empower) that supply the gain in each of the matched amplifiers, together with the oscillator pulse spacing. Tuning of the pump timing allows arbitrary selection of output pulse spacing down to $\sim$12 ns, as determined by the free spectral range of the oscillator.

Beam combining optics direct the output of the three laser amplifiers into a single beam path where the alignment and the spatial and temporal profiles of each pulse are adjusted to provide three matched pulses. This pulse train is directed to a beamsplitter which separates a portion of each source pulse in order to drive the optical (Kerr effect) shutter which is used to select a specific 1.5 ps temporal slice of each imaging pulse. The divided pulses proceed along two beam paths: an imaging beam and a switching beam, which cross inside the Kerr cell (see

fig. 1b). The remaining source light (imaging beam) is directed through the measurement volume, where it probes the structure of the region under investigation, and then proceeds through the collection optics, optical shutter, and detection system.

As fig. 1 indicates, the signal is collected in a forward-scatter geometry, effectively imaging light from a thin object plane (∼50 μm) in the measurement volume to the sensor at near unit magnification. Here, the signal is collected by an achromatic doublet (f/5.9) in a 2f-arrangement [9], and a large relative aperture, focal length, sensor size, and short object distance are maintained to provide a short depth-of-field which can be exploited to spatially resolve the focused image content.

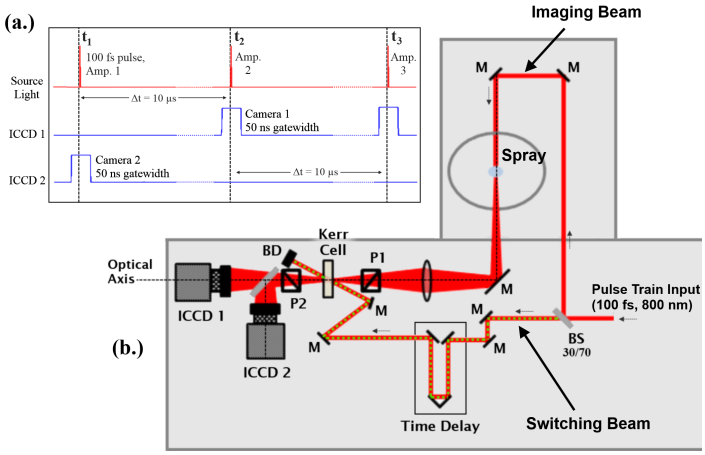

Fig. 1. (a.)Timing diagram and (b.) imaging setup for 3-pulse time-gated ballistic imaging (M:mirror, P:polarizer, BS:beam splitter, BD:beam dump, ICCD:intensified camera). Source light from three amplifiers is combined to provide a high-energy train of three ultrafast pulses. Each source pulse is split into *imaging* and *switching* paths to drive the Kerr-effect shutter (OKE-Gate) and generate one ballistic image.

Prior to detection, the image signal is filtered by a Kerr effect time-gate. This optically driven shutter consists of a pair of crossed polarizers which bracket a glass cell containing liquid carbon disulfide (CS_2). Here, the light which was divided from each pulse (switching beam) is directed and path-length matched to overlap with its corresponding imaging pulse. In this "crossed-beam" arrangement, the switching beam intersects with the imaging path at an angle of ∼14° within the Kerr cell as it propagates along the optical axis of the imaging system. A delay-stage placed in the switching beam path provides adjustable control of the overlap between the switching and imaging pulses.

The intense electric field of the switching pulse serves to align the dipoles of the CS_2 in the Kerr medium, giving rise to a Kerr effect birefringence which quickly dissipates when the switching pulse is no longer present [10]. Kerr effect gating can be realized with many materials, but the transparency and strong Kerr response of CS_2 along with its fast relaxation time (∼1.5 ps) make it suitable for constructing efficient gating elements [11]. The timing of the induced Kerr effect birefringence can be adjusted by changing the relative length of the beam paths and, together with the action of the crossed polarizers, this allows the selection of an ultrashort (∼1.5 ps) section of the imaging pulse. Since the timing of the shutter is controlled by the optical path following the beamsplitter, this gating effect proceeds identically for each source pulse which transits the system.

Final collection of high-quality imaging light from each source pulse is effected by dividing the optical signal exiting the Kerr gate into two detection paths with dedicated camera hardware. Images are acquired by two interline-transfer CCD cameras equipped with fiber-coupled intensifiers (Princeton Instruments, PI-Max4). The gain response of the intensifiers can be gated to 5 ns and, with masked storage and specialized readout, the camera hardware is able to generate two images separated by as little as 450 ns. Thus, the exposure, intensifier, and transfer timings for each camera can be set to capture consecutive image pulses (two images per camera).

With this arrangement, each pulse train yields three time-correlated images of the spray. The Chalmers steady spray rig was used to set up a controlled test case for measuring fluid velocity and acceleration in a turbid environment. Image-triplets of a water spray (P_{inj} = 19 bar) exiting a plain-orifice nozzle (L/d = 25) were acquired for dynamic BI analysis. One such image triplet is shown in fig. 2. Here the flow is from top to bottom and the images each capture an 8.6 mm field-of-view (9 μm/pixel) situated 28 mm below the orifice.

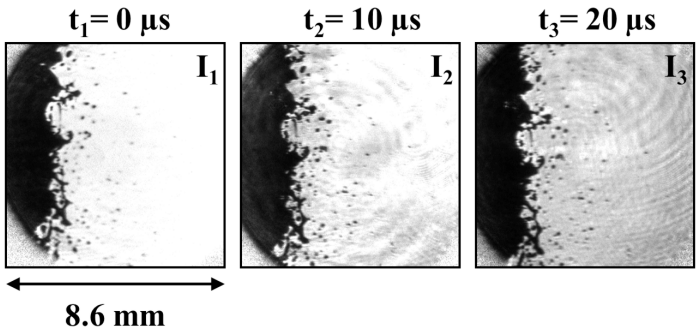

Fig. 2. Time-correlated ballistic images showing breakup in a turbulent spray 28 mm below the (6 mm dia.) nozzle. The view includes the spray periphery and the flow is from top to bottom (flowrate ∼ 60 lpm). Images I_1, I_2, and I_3, show same 8.6 mm field-of-view at 10 μs intervals.

In its current configuration, the ultimate time-resolution of the multi-pulse imaging system is limited by the intensifier response. Note that while the phosphor of the intensifier has a relatively short decay time (<3% by ∼350 ns), the BI images can be sensitive to ghosting at several times this value due to the lower dynamic range of the filtered signal. For this work our testing showed interframe cross-talk was negligible at a frame spacing of ∼500 ns.

Images from the two cameras are corrected to correspond to the same spatial scale and coordinate system by applying a geometric transform computed from test images of a static grid target placed at the system object plane [12]. In addition, a shadowing correction [13] and background subtraction is applied to the raw ballistic images, producing a normalized series of three images with uniform coordinates for each pulse train.

The main object of the 3-pulse BI system is to enable the acquisition of spatially-resolved time-series data that can be analyzed to track motion and changes in the imaged structure. Consecutive images in the series are compared and velocity vectors are computed for each time-step by selectively matching structure from targeted image regions. By computing coordinated sets of velocity vectors, time-resolved displacement information ac-

quired from multiple time-steps can be used to estimate higher-order motion components. As in previous work, the underlying matching analysis relies on normalized cross-correlation of resolved image structure [14]. However, in the present case, three images taken at times t_1, t_2, and t_3 are processed to generate two matched sets of velocity data which correspond to the (equal) time intervals, [t_1, t_2] and [t_2, t_3]:

$$\Delta t = t_2 - t_1 = t_3 - t_2 = 10\ \mu\text{s} \quad \textbf{(1)}$$

Velocity analysis proceeds by selecting two images, I_1 and I_2 separated by time, Δt. A Canny filter is applied to identify edges in I_1, which are used to position regularly spaced arrays of initial target points near image regions which contain trackable features. These targets are used to sample rectangular subregions of image data (templates) containing the structural information to be tracked. Larger rectangular subregions (search fields) are selected from I_2 using the same target coordinates, and the cross-correlation is calculated for each of the corresponding template and search field pairs. Displacement vectors are generated for each pair to make up a set of vectors, v_1, where the offset between each set of template coordinates and its best match coordinates in the corresponding search field are indicated by the maximum value of the correlation function.

This matching procedure carries the implicit assumption that the referenced intensity data correspond to spatially resolved structure. In general, simple integration of the full transmitted signal in a forward-scatter system results in a projected shadow with no definite restriction along the measurement axis. However, the addition of imaging optics alters the efficiency of light collection— skew light rays are cut off by the stops and apertures of the optical components, while light with angular paths accepted by the collection optics continues to the image plane. Light focusing by the collection and camera lenses further modifies this angular propagation, producing the familiar Fourier relationship between collected and focused light which emphasizes spatial content from the object plane when it's properly imaged (inverse transformed). The steepness of this efficiency is expressed by the imaging system depth-of-field (DoF) [15]. In the present system, correlation errors are minimized by maintaining a shallow DoF ($\sim$50 μm), and automatic exclusion of target regions which contain only low spatial frequency content. Figure 3 shows a set of vectors computed from images I_1 and I_2 (shown in fig. 2) with corresponding time step, [t_1, t_2].

Given properly sized search field and template regions, and significant variation in the template spatial intensity, the computed displacements indicate the motion of the underlying fluid structure during the interframe time step, [t_1, t_2]. In addition, validation criteria are applied to ensure the quality of individual velocity vectors by discarding classes of matches with high probability of error, such as matches at boundaries, or low coefficient matches. Sedarsky, et al. [16] provide more detail on these validation criteria as well as concerns for window sizing.

Velocity analysis continues for the next time-step by selecting images, I_2 and I_3, which are separated by the same relative time, Δt, as the first image-pair. Here, the final match coordinates for displacements in the previous time-step are used to specify targets, and these target pixels are used to position template and search field regions. The analysis proceeds as before, correlating structure sampled from I_2 within search field data sampled from I_3. This yields a second set of velocity vectors, v_2, which are spatially coincident with the vectors computed in the previous time-step.

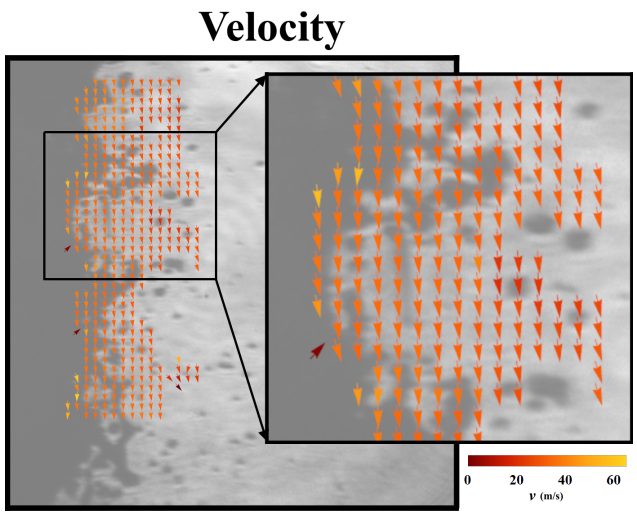

Fig. 3. Correlation results computed from target regions (75x75) in images I_1 and I_2, as shown in fig. 2. Vector magnitude indicated by color: red represents lowest velocity, yellow represents highest velocity, $\sim$65 m/s^2.

It is worth noting that, assuming accurate data, the discrete time-resolved displacement computed by the velocity analysis actually corresponds to the average velocity over that sampling interval. Consequently, velocities for each time-step are more accurately defined by linearized representative times which can be written:

$$t_{v1} = \tfrac{1}{2}(t_1 + t_2) \quad \textbf{(2)}$$

$$t_{v2} = \tfrac{1}{2}(t_2 + t_3) \quad \textbf{(3)}$$

where t_{v1} and t_{v2} correspond to times for the [t_1, t_2] and [t_2, t_3] velocity sets, respectively.

Acceleration is the instantaneous rate of change of velocity with respect to time. In the limit of small time-steps, such that fluid distortion is negligible, the acceleration of fully time-resolved fluid structures is given by:

$$a = \frac{du_i}{dt} \approx \frac{v_i(t+\Delta t) - v_i(t)}{\Delta t} = \frac{v_{2,i} - v_{1,i}}{\frac{1}{2}(t_1 + t_2) - \frac{1}{2}(t_2 + t_3)} \quad \textbf{(4)}$$

where the lowercase subscript, i, denotes summation over Cartesian spatial coordinates, v represents velocity as a function of time, t, and v_1 and v_2 represent discrete velocity components with corresponding times t_{v1} and t_{v1}, as given by eqs. 2 and 3.

Using the coordinated sets of velocity vectors, v_1 and v_2, derived from the series of three images, 2D acceleration vectors can be computed by applying eq. 4 to matched pairs of discrete velocity values. Provided that densities remain constant within the associated windows, the result is a set of acceleration vectors which form a first-order estimate of the forces acting on the fluid structure. Figure 4 shows a field of arrows representing acceleration vectors acting on fluid structures as the jet breaks apart. Note that while these particular results are derived from images of spray breakup, the analysis discussed here applies equally to time-gated BI in other turbid media in all cases where the measurement data allow sufficient image resolution and contrast for valid correlation matching.

A rough estimate of the uncertainty in the acceleration determined by correlation matching, as described above, can be

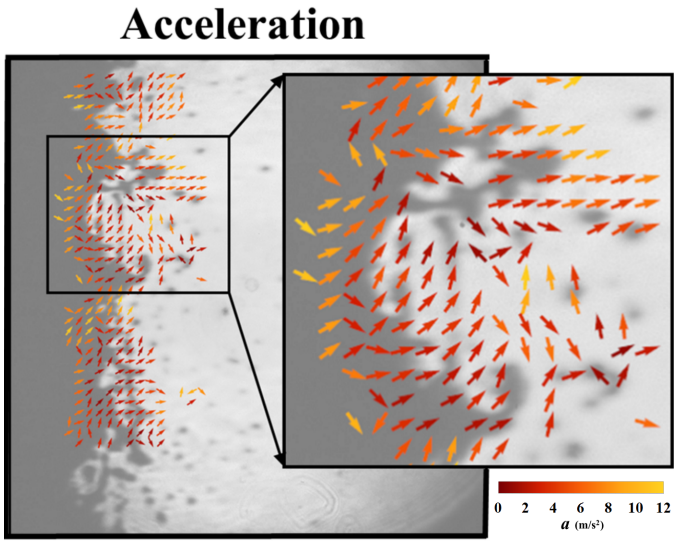

Fig. 4. Acceleration vectors representing motion and forces involved in spray development, computed from time-correlated ballistic images. Color scale represents vector magnitude, red represents lowest acceleration, and yellow represents highest acceleration (~12 m/s^2).

generated by modeling the procedure in terms of a stochastic process [17]. Here, the intermediate velocity vectors can be viewed as individual steps in a Markov chain, with states defined by the speed and motion of correlated structure over spatial coordinates, (x,y). Considering that vectors for times t_{v1} and t_{v2} are computed through identical processes, one can assume statistics of neighbor states may serve as a crude prior state model. Thus, v_1 serves as the prior for v_2, and in the limit of short time-steps such that the losses are negligible, a time-reversed v_2 can serve as the v_1 prior. Since the constituent vectors for the acceleration are spatially coincident (v_1 endpoints match v_2 startpoints), the parameters of each state depend only on the (x,y) components of the vectors in the sets, v_1 and v_2. In the absence of specific knowledge about the shape of the errors, it is reasonable to assume that the validated correlation results represented by the sets, v_1 and v_2, correspond to a random variation with normally distributed values. Here the mean and variance can be defined from the (integer pixel valued) priors, validation criteria and template window size constraints. Recalling that the distribution of a difference of two normally distributed variates is also a normal distribution, it follows that the random variation in each spatial dimension (e.g. from the form of the correlation peak, spatial aliasing, discretization, etc.) can be expressed as:

$$P_{v2-v1}(u) = \frac{\exp\left[-(u-(\mu_{v2}-\mu_{v1}))^2/2(\sigma_{v2}^2+\sigma_{v1}^2)\right]}{\sqrt{2\pi(\sigma_{v2}^2+\sigma_{v1}^2)}} \quad (5)$$

where μ_{v1}, σ_{v1} and μ_{v2}, σ_{v2} are the respective means and standard deviations of vector sets v_1 and v_2. Applying this error model results in σ=4 pixels in the y-direction and σ=2 pixels in the x-direction; extending this result to acceleration yields magnitude and pointing uncertainties of $\pm$4 m/s^2 and 5°, respectively.

Velocity results for the spray indicate large streamwise motion with small variations in the radial direction. The results exhibit the expected radially decreasing velocity profile, with higher velocities near the liquid core. The median axial velocity calculated from the correlation is ~37 m/s. A typical acceleration result is shown in fig. 4. Here it is apparent that the liquid structures are subjected to acceleration in the positive radial direction, and retardation in the streamwise direction. This indicates both turbulence and shear forces affecting the breakup of the liquid jet. The median radial acceleration is 2.6 m/s^2 and the axial acceleration is -1.7 m/s^2.

ACKNOWLEDGEMENTS

The authors acknowledge the Swedish Research Council, the Swedish Energy Agency, and the Knut and Alice Wallenberg Foundation for funding this work.

REFERENCES

1. W. Schröer, J. Köser, and F. Kuhnen, "Light–scattering in turbid fluids: The single-scattering intensity," Journal of Molecular Liquids **134**, 40–48 (2007).
2. M. I. Mishchenko, "Multiple scattering, radiative transfer, and weak localization in discrete random media: Unified microphysical approach," Reviews of Geophysics **46**, RG2003 (2008).
3. E. Berrocal, D. L. Sedarsky, M. E. Paciaroni, I. V. Meglinski, and M. A. Linne, "Laser light scattering in turbid media Part I: Experimental and simulated results for the spatial intensity distribution," Optics Express **15**, 10649 (2007).
4. B. B. Das, K. M. Yoo, and R. R. Alfano, "Ultrafast time-gated imaging in thick tissues: a step toward optical mammography," Optics Letters **18**, 1092 (1993).
5. T. Baumgart, S. T. Hess, and W. W. Webb, "Imaging coexisting fluid domains in biomembrane models coupling curvature and line tension," Nature **425**, 821–824 (2003).
6. V. Bianco, M. Paturzo, O. Gennari, A. Finizio, and P. Ferraro, "Imaging through scattering microfluidic channels by digital holography for information recovery in lab on chip," Optics Express **21**, 23985 (2013).
7. M. Linne, "Imaging in the optically dense regions of a spray: A review of developing techniques," Progress in Energy and Combustion Science **39**, 403–440 (2013).
8. T. D. Fansler and S. E. Parrish, "Spray measurement technology: a review," Measurement Science and Technology **26**, 012002 (2015).
9. M. Rahm, M. Paciaroni, Z. Wang, D. Sedarsky, and M. Linne, "Evaluation of optical arrangements for ballistic imaging in sprays," Optics Express **23**, 22444 (2015).
10. P. P. Ho and R. R. Alfano, "Optical Kerr effect in liquids," Physical Review A **20**, 2170–2187 (1979).
11. R. A. Ganeev, A. I. Ryasnyansky, M. Baba, M. Suzuki, N. Ishizawa, M. Turu, S. Sakakibara, and H. Kuroda, "Nonlinear refraction in CS2," Applied Physics B **78**, 433–438 (2004).
12. M. Alghoniemy and A. H. Tewfik, "Geometric distortion correction in image watermarking," (International Society for Optics and Photonics, 2000), pp. 82–89.
13. T. C. Williams and C. R. Shaddix, "Simultaneous correction of flat field and nonlinearity response of intensified charge-coupled devices," Review of Scientific Instruments **78**, 123702 (2007).
14. D. Sedarsky, J. Gord, C. Carter, T. Meyer, and M. Linne, "Fast-framing ballistic imaging of velocity in an aerated spray," Optics Letters **34**, 2748–2750 (2009).
15. D. Sedarsky, S. Idlahcen, J.-B. Blaisot, and C. Rozé, "Planar velocity analysis of diesel spray shadow images," arXiv:1203.5347 [physics] (2012). ArXiv: 1203.5347.
16. D. Sedarsky, S. Idlahcen, C. Rozé, and J.-B. Blaisot, "Velocity measurements in the near field of a diesel fuel injector by ultrafast imagery," Experiments in Fluids **54**, 1–12 (2013).
17. J.-L. Gauvain and Chin-Hui Lee, "Maximum a posteriori estimation for multivariate Gaussian mixture observations of Markov chains," IEEE Transactions on Speech and Audio Processing **2**, 291–298 (1994).